Available online at www.sciencedirect.com
ScienceDirect
Journal of Power Sources 173 (2007) 249–263
JOURNAL OF POWER SOURCES
www.elsevier.com/locate/jpowsour

Flow distribution in the manifold of PEM fuel cell stack

Chung-Hsien Chen [a,*], Shiauh-Ping Jung [b], Shi-Chern Yen [a]

[a] *Department of Chemical Engineering, National Taiwan University, Taiwan*
[b] *Energy and Environment Research Laboratories, ITRI, Taiwan*

Received 9 April 2007; received in revised form 3 May 2007; accepted 3 May 2007
Available online 7 May 2007

Abstract

In this study, the pressure variation and the flow distribution in the manifold of a fuel-cell stack are simulated by a computational fluid dynamics (CFD) approach. Two dimensional stack model composed of 72 cells filled with porous media is constructed to evaluate pressure drop caused by channel flow resistance. In order to simplify this model, electrochemical reactions, heat and mass transport phenomena are ignored and air is treated as working fluid to investigate flow distribution in stacks. Design parameters such as the permeability of the porous media, the manifold width and the air feeding rate were changed to estimate uniformity of the flow distribution in the manifold. A momentum-balance theory and a pressure-drop model are presented to explain the physical mechanism of flow distribution. Modeling results indicate that both the channel resistance and the manifold width can enhance the uniformity of the flow distribution. In addition, a lower air feeding rate can also enhance the uniformity of flow distribution. However, excessive pressure drop is not beneficial for realistic applications of a fuel-cell stack and hence enhanced manifold width is a better solution for flow distribution.

Keywords: Fuel cell; Stack; Manifold; Porous media; Gas pressure; Flow distribution

1. Introduction

A proton exchange membrane (PEM) fuel cell is an electrochemical device where chemical energy is directly converted into electricity by using hydrogen as fuel and oxygen as oxidant [1]. A single PEM fuel cell can offer a voltage of ∼0.6–0.7 V. In order to increase the voltage sufficient for practical operations, many single cells are serially connected to fabricate the fuel-cell stack. Sufficient reactant feed is necessary for each cell to attain high performance and stable operation of stacks. The gas manifolds play a key role in the uniform distribution of reactant gases to the individual cells. A good manifold design is important to achieve the above requirement. An uneven flow distribution will result into performance loss as well as the stack may cease to function.

Till now most of the PEM fuel cell modeling works mainly focus on electrochemical, heat and mass transport phenomena in a single cell. The single cell models reported by Bernardi and Verbrugge [2,3], Springer et al. [4], Nguyen and White [5], Gurau et al. [6], are some of the examples. Recently, the Pennsylvania State University [7–12] in the US and University of Victoria [13–15] in Canada are reporting impressive modeling job.

The above mentioned single cell models deal with the construction of the fuel cell model based on the numerical techniques to simulate the related phenomena that occur within the fuel cell. The model parameters are normally verified with the experimental results. The models help to predict the performance characteristics and understand the physical phenomena that occur within the fuel cell.

In recent years, increasing number of researchers are focusing on the modeling of fuel-cell stack. The models are mainly focusing on the flow distribution and water-thermal management of stacks. Usually, the modelers ignore the complicated issues like electrochemistry and transport process in order to simplify the models. Koh et al. [16] have reported a numerical model to investigate pressure variation and flow distribution of stacks. This model considers channels filled with porous media to evaluate pressure drop caused by channel configuration. In addition, it compares flow distribution for different overall gas flow patterns. Karimi et al. [17] have developed a stack model with fluid

* Corresponding author. Tel.: +886 2 27757620; fax: +886 2 27757728.
E-mail addresses: ctchen62@ntu.edu.tw, d89524015@ntu.edu.tw (C.-H. Chen).

0378-7753/$ – see front matter © 2007 Elsevier B.V. All rights reserved.
doi:10.1016/j.jpowsour.2007.05.007

Nomenclature

a	link coefficient
$\vec{F}_f$	wall shear force (N)
K	permeability (m^2)
$\dot{m}$	mass flow rate ($kg\,s^{-1}$)
n	normal direction relative to outlet ports
N	number of cells
$\dot{p}$	production rate of κ ($m^2\,s^{-3}$)
P	pressure (Pa)
$\dot{Q}$	total mass flow rate of stacks ($kg\,s^{-1}$)
S	source term
$\vec{S}$	pressure action area (m^2)
t	time (s)
T_{in}	turbulence intensity
U	velocity vector ($m\,s^{-1}$)
$\vec{V}$	velocity vector ($m\,s^{-1}$)
x	Cartesian coordinates (m)

Greek letters

Φ	physical value
Γ	exchange coefficient
δ	tensor
ε	turbulent dissipation rate ($m^2\,s^{-3}$)
ϕ	porosity
κ	turbulent kinetic energy ($m^2\,s^{-2}$)
μ	viscosity ($kg\,m^{-1}\,s^{-1}$)
ρ	density ($kg\,m^{-3}$)
τ	shear stress ($N\,m^{-2}$)

Subscripts and superscripts

C	empirical constants
eff	effective property which accounts for porosity
in	inlets
i,j	components of a vector in Cartesian coordinates
sys	system
t	turbulent
σ	empirical constants
ϕ	general dependent variable

mechanics method. Reactant species such as hydrogen, oxygen, nitrogen, etc. were introduced into this model so that it can evaluate the relationship between the consumption rate of reactants and stack output power. Yu et al. [18] have proposed a water-thermal management model to investigate PEM fuel-cell stacks made from Ballard power system, Canada. This model can predict temperature, voltage, power, efficiency, etc. under steady and transient operations of stacks, respectively. Promislow and Wetton [19] proposed a steady heat transfer model of PEM fuel-cell stacks composed of parallel cooling channels and infinitely thin membrane electrode assembly (MEA). This model predicts not only the local temperature difference between coolant and MEA, but also the cell temperature variation.

The stack modeling mentioned above is mainly concerned with developing a numerical model characterizing gas flow distribution and water-thermal management. The above models were based on numerical analysis but not on computational fluid dynamics. These models could not investigate detailed stack flow field configuration and transport phenomena. Although simplified models can evaluate stack performance characteristics rapidly, it is also possible to obtain wrong results due to the over-simplification of the model.

Experimental data associated on the gas or coolant flow distribution is usually difficult to obtain. Therefore, indirect measurements like voltage or temperature distribution are used to understand the physical phenomena that occur in a fuel-cell stack. Due to the lack of experimental data, fuel-cell stack numerical models only provide theoretical explanations and understanding about performance characteristics. In this study, since there is no appropriate experimental data available, physical mechanism about flow distribution is investigated only by using purely theoretical approach. But it is indeed an available and acceptable method for studying phenomena that could not be experimentally measured or calculated.

This study presents a computational fluid dynamics model of PEM fuel-cell stack to investigate pressure variation and flow distribution. A two-dimensional model consisting of 72 channels filled with porous media is implemented for the theoretical analysis. The momentum balance theories proposed can explain pressure variation and pressure drop model can characterize the correlation between pressure variations and flow distribution. In addition, the influences of design parameters on flow distribution regarding channel flow resistance, manifold width and air feed rate will be discussed in detail.

2. Mathematical model

Stack two-dimensional model is shown in Fig. 1(a) and (b). The gases enter manifolds through inlet ports, and then are distributed into each cell and reach the electrodes through diffusion. After the electrochemical reactions are completed, un-reacted gases and products are discharged into manifolds from cells and then leave stacks through outlet ports. This flow field networks constitute an overall gas transport path. Besides simplifying stacks into two-dimensional model, other basic assumptions are as follows:

1. the flow is steady;
2. the flow is turbulent;
3. the incompressible air is used as working fluid;
4. electrochemistry, heat and mass transport phenomena are ignored;
5. the gravity force is ignored and reference pressure for 1 atm is set; and
6. the channels are filled with porous media.

Flow-field governing mechanism considered is turbulent. In order to simulate turbulent flow, κ–ε model is used to solve related transport equations. In addition, since channels are filled with porous media, treatment of porous media flow analysis is considered within turbulent model [20]. Governing equations are given as below:

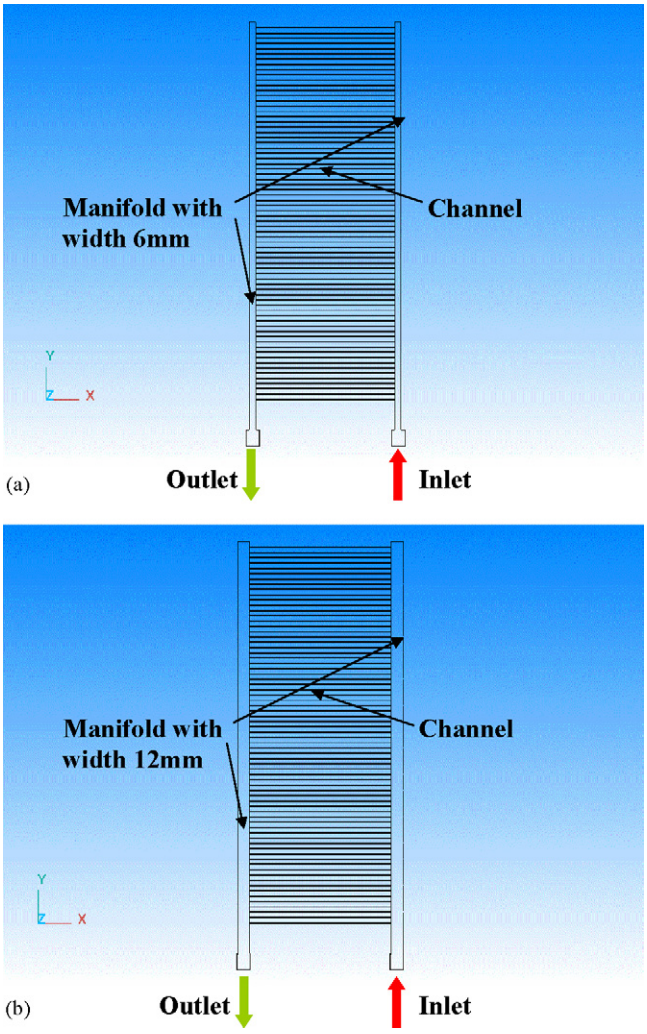

Fig. 1. Schematic representation of fuel-cell stacks with manifold width (a) 6 mm, (b) 12 mm.

Continuity equation:

$$\nabla \times (\phi U) = 0 \tag{1}$$

Momentum equation:

$$\rho \nabla \times (\phi U U) = -\phi \nabla p + \nabla \times (\phi \tau) + \frac{\phi^2 \mu U}{K} \tag{2}$$

$$\tau = \frac{\partial}{\partial x_j}\left\{\mu\left(\frac{\partial U_i}{\partial x_j} + \frac{\partial U_j}{\partial x_i}\right) - \frac{2}{3}\rho\kappa\delta_{ij}\right\} \quad \begin{matrix}\delta_{ij} = 1 & \text{if } i = j \\ \delta_{ij} = 0 & \text{if } i \neq j\end{matrix} \tag{3}$$

where κ is turbulent kinetic energy;

κ (turbulent kinetic energy) equation:

$$\rho \nabla \times (\phi U \kappa) = \nabla \times \left(\mu + \frac{\mu_t}{\sigma_\kappa} \nabla (\phi \kappa)\right) + \dot{p} - \rho(\phi\varepsilon) + c_k \rho \phi^2 \frac{\kappa |U|}{\sqrt{K}} \tag{4}$$

where κ is turbulent kinetic energy, $\dot{p} = -\rho\phi(\overline{U_i' U_j'})(\partial(\phi U_i)/\partial x_j)$ is production rate of κ, ε is turbulent dissipation rate, $c_k \rho \phi^2 (\kappa |U|/\sqrt{K})$ is additional production rate of κ caused by porous media. $\sigma_\kappa = 1.0$ and $c_k = 0.28$ are empirical constants.

ε (turbulent dissipation rate) equation:

$$\rho \nabla \times (\phi U \varepsilon) = \nabla \times \left(\mu + \frac{\mu_t}{\sigma_\varepsilon} \nabla (\phi \varepsilon)\right) + C_{\varepsilon 1} \frac{\varepsilon}{\kappa} \dot{p} + C_{\varepsilon 2} \rho \phi \left(c_k \frac{\varepsilon |\phi U|}{\sqrt{K}} - \frac{\varepsilon^2}{\kappa}\right) \tag{5}$$

where $\sigma_\varepsilon = 1.3$, $C_{\varepsilon 1} = 1.44$, $C_{\varepsilon 2} = 1.92$ are empirical constants.

In the above governing equations, ϕ is porosity and K is permeability of porous media. For the flow in the porous media, namely channel flow, ϕ is between 0 and 1 and K is a finite value depending on properties of porous media. For clear fluid flow, namely manifold flow, ϕ is equal to one and K approaches infinitely large. At this stage, flow field will be entirely filled with fluid without the existence of porous media.

The boundary conditions imposed to the boundaries of the computational domain are described as follows. The two air-feeding rates used are 100 and 300 standard liters per minute (SLPM). Air inlet velocity can be calculated from the feeding rate. Other boundary conditions are given as follows:

Inlet boundary conditions:

1. air average velocities at inlet ports are 3 m s^{-1} and 9 m s^{-1}, respectively;
2. κ and ε can be defined as follows:

$$\kappa = \frac{3}{2}(U_{\text{in}} T_{\text{in}})^2; \qquad \varepsilon = C_\mu^{3/4} \frac{\kappa^{3/2}}{\lambda}, \qquad \lambda = 0.07L \tag{6}$$

where U_{in} is inlet velocity, T_{in} is turbulence intensity with value 0.1, L is hydraulic diameter with value 15 mm.

Outlet boundary conditions are:

1. outlet pressure is constant at 1 atm;
2. fully developed flow at outlet ports, i.e. $\partial \Phi/\partial n = 0$, where n indicates normal direction relative to outlet ports, Φ represents physical properties such as velocities, pressure, etc.

Wall boundary conditions:

1. flow is considered not to slip at wall therefore wall fluid velocity is zero;
2. wall function is adopted to simulate turbulent wall shear stress.

Since it is impossible to obtain an analytic solution of the complex convection-diffusion problem like this one, it will be solved by a finite volume method using a collocated cell-centered variable arrangement. The governing equations can be expressed in the form of a generalized transport equation

$$\nabla \times (\rho \vec{u} \phi - \Gamma_\phi \nabla \phi) = S_\phi \tag{7}$$

where ϕ is the general dependent variable, Γ_ϕ the exchange coefficient, S_ϕ the source term, $\vec{u}$ velocity vector, and ρ is density.

With the discritization of the governing equations, the coupled finite-difference equations become

$$a_P\phi_P = a_E\phi_E + a_W\phi_W + a_N\phi_N + a_S\phi_S + S_\phi \quad (8)$$

where ϕ_P is the value of ϕ at the current point P, $\phi_E \ldots \phi_S$ stand for the values of the grid points adjacent to the point P, and $a_P \ldots a_S$ are known as the link coefficients.

In this study, ESI-CFD ACE+ computational-fluid-dynamics software is used as modeling tools. The model is based on finite volume method, where the solution algorithm is SIMPLEC (Semi-Implicit Method for Pressure-Linked Equation Consistent) proposed by Van Doormal and Raithby [21] in 1984. Compared with SIMPLE (Semi-Implicit Method for Pressure-Linked Equation) developed by Patankar [22], SIMPLEC algorithm can provide quicker and more effective convergent solutions.

Computational domains are divided into appropriate number of meshes. Through this discretization process differential governing equations are transformed into algebraic equations on computational meshes. For computational accuracy and stability, locally dense meshes should exist in specific domains with dramatically varied properties, such as channels, variable flow cross-sectional area or flow-field turns. According to grid tests, a body-fitted grid with 85000 computational cells is appropriate under compromise between modeling economy and reliability.

In addition, continuity, momentum, turbulent kinetic and turbulent dissipation rate equations are solved in turn until the iterative process meets the convergence criteria. In this study, definition of convergence criteria indicates that the largest relative error between consecutively two iterative residuals within overall computational domains is less than 10^{-4}.

3. Results and discussions

Using an advanced fuel-cell stack test station, overall output current, power, reactant flow rate, pressure drop, cell voltage, temperature distribution, etc. can be easily measured. As for reactant or coolant distribution, experimental device and technique are generally difficult to implement so these microscopic phenomena have not yet been observed clearly. Some methods such as voltage distribution measurement can provide indirect information about reactant flow distribution. For example, while some cells in a stack produce lower voltage than others, it is possible that less reactant is fed into the cells with low voltage. But other effects such as flooding or local overheating also might be the reason for the voltage loss.

Physical mechanisms of flow distribution in stacks are discussed and uniform degree of flow distribution is evaluated by changing design parameters. These parameters are included in channel flow resistance, manifold width and air feeding rate. Generally, channels with large flow resistance can cause large pressure drop and better performance in fuel cells. Channel flow resistance contributes mostly to pressure drop, but it is still not clear how channel flow resistance influences flow distribution. In this study, different channel flow resistances caused by adjusting permeability of porous media are analyzed to evaluate flow distribution. Manifolds are paths of reactant feed and discharge in fuel cell stacks. The geometrical size of manifold cross-sectional area will influence overall pressure drop in stacks but its effects on flow distribution is still not clearly known. In order to understand how flow distribution is affected by manifold width, different manifold sizes are used to evaluate this effect. In addition, this paper will also study the influence of different air feed on flow distribution. The model parameters and modeling conditions are given in Table 1. The cases analyzed in this study are shown as below:

Table 1
Stack model parameters and modeling conditions

Variable	Value
Number of cells	72
Gas channel depth (mm)	0.8
Cell-to-cell distance in manifold axis (mm)	6
Manifold width (mm)	6 and 12
Width of inlet and outlet holes (mm)	15
Porosity in cell channel	0.4
Gas permeability in cell channel (m^2)	2.5×10^{-10} and 2.5×10^{-9}
Back pressure (atm)	1
Air flow rate (SLPM)	100 and 300
Air viscosity ($kg\,m^{-1}\,s^{-1}$)	1.846×10^{-5}
Air density ($kg\,m^{-3}$)	1.1614

Case 1: permeability $K = 2.5 \times 10^{-10}$, manifold width $D = 6$ mm
Case 2: permeability $K = 2.5 \times 10^{-10}$, manifold width $D = 12$ mm
Case 3: permeability $K = 2.5 \times 10^{-9}$, manifold width $D = 6$ mm
Case 4: permeability $K = 2.5 \times 10^{-9}$, manifold width $D = 12$ mm

Permeability of porous media can approximate the pressure drop in the channels. If the permeability is lower, pressure difference will be higher in the channels. Therefore, pressure drops caused by different channel configuration are realized when the permeability is varied, i.e. the channel flow resistance is varied. By changing this parameter, the influence of channel flow resistance on flow distribution can be investigated. There is one order magnitude of difference for permeability in these cases so there will also be approximately one order magnitude of difference for the overall pressure drop. Larger deviation between magnitudes of permeability can cause a more apparent difference of flow distribution. That is why we choose cases with permeability $K = 2.5 \times 10^{-10}$ and $K = 2.5 \times 10^{-9}$. In addition, this study also evaluates how different manifold widths influence flow distribution. Manifold widths of 6 mm and 12 mm are evaluated and 6 mm is the origin design in stacks. In order to observe the apparent effect of manifold width to flow distribution, cases where size of origin width are doubled, i.e. 12 mm, are investigated. In the following section, flow pressure variation, channel pressure drop and cell flow rate under 300 SLPM air feeding rate will be discussed separately.

3.1. Flow pressure in stacks

Flow pressure variations of case 1, case 2, case 3 and case 4 under 300 SLPM air feeding rate are shown in Figs. 2–4 and Fig. 5(a)–(c), respectively where (a) is overall flow pressure in stacks and (b) and (c) are respectively average pressure variation along inlet and outlet manifold length.

For overall flow pressure in stacks, i.e. the right hand side of Figs. 2–5, the highest pressure occurs in the inlet manifold and the lowest one in the outlet manifold. In channels, pressure gradually decreases from the inlet manifold to the outlet one. On comparing the overall pressure drop of each case, case 1 > case 2 > case 3 > case 4. This shows that the increased channel flow resistance due to lower permeability contributes to a larger overall pressure drop. As mentioned earlier, the pressure drop in stacks is mainly controlled by the permeability i.e. $K = 2.5 \times 10^{-10}$ (case 1 and case 2) and $K = 2.5 \times 10^{-9}$ (case 3 and case 4). These results show that one order decrease of magnitude for permeability will increase the overall pressure drop by about one order magnitude, i.e. pressure drop increases from 3377 Pa (case 4) and 4003 Pa (case 3) to 29540 Pa (case 2) and 30160 Pa (case 1).

Larger manifold widths cause less overall pressure drop. While manifold width increases from 6 mm (case 1 and case 2) to 12 mm (case 3 and case 4), the overall pressure decreases from 4003 Pa (case 3) and 30160 Pa (case 1) to 3377 Pa (case 4) and 29540 Pa (case 2). According to fluid mechanics theories, lowered fluid velocity due to enhanced manifold width will contribute to less pressure drop.

On the left hand side of the figures, the top plot is pressure variation along the inlet manifold and the bottom one is pressure variation along the outlet manifold. The x-coordinate indicates distance along manifold length where the origin is at the feeding end of stacks, and the y-coordinate is pressure

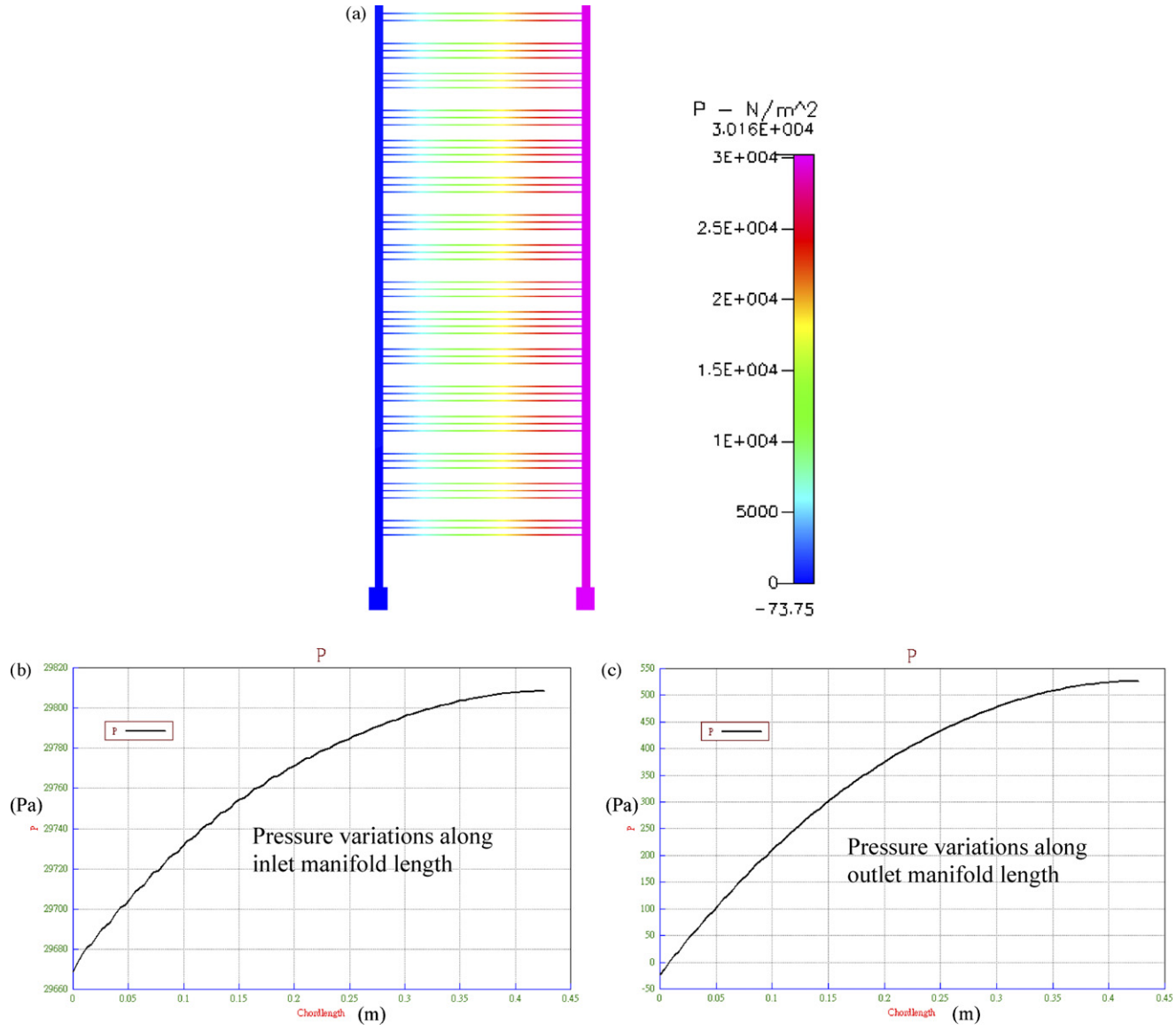

Fig. 2. (a) Stack flow pressure, (b) pressure variations along inlet manifold length, (c) pressure variations along outlet manifold length for case 1 ($K = 2.5 \times 10^{-10}$, $D = 6$ mm, 300 SLPM).

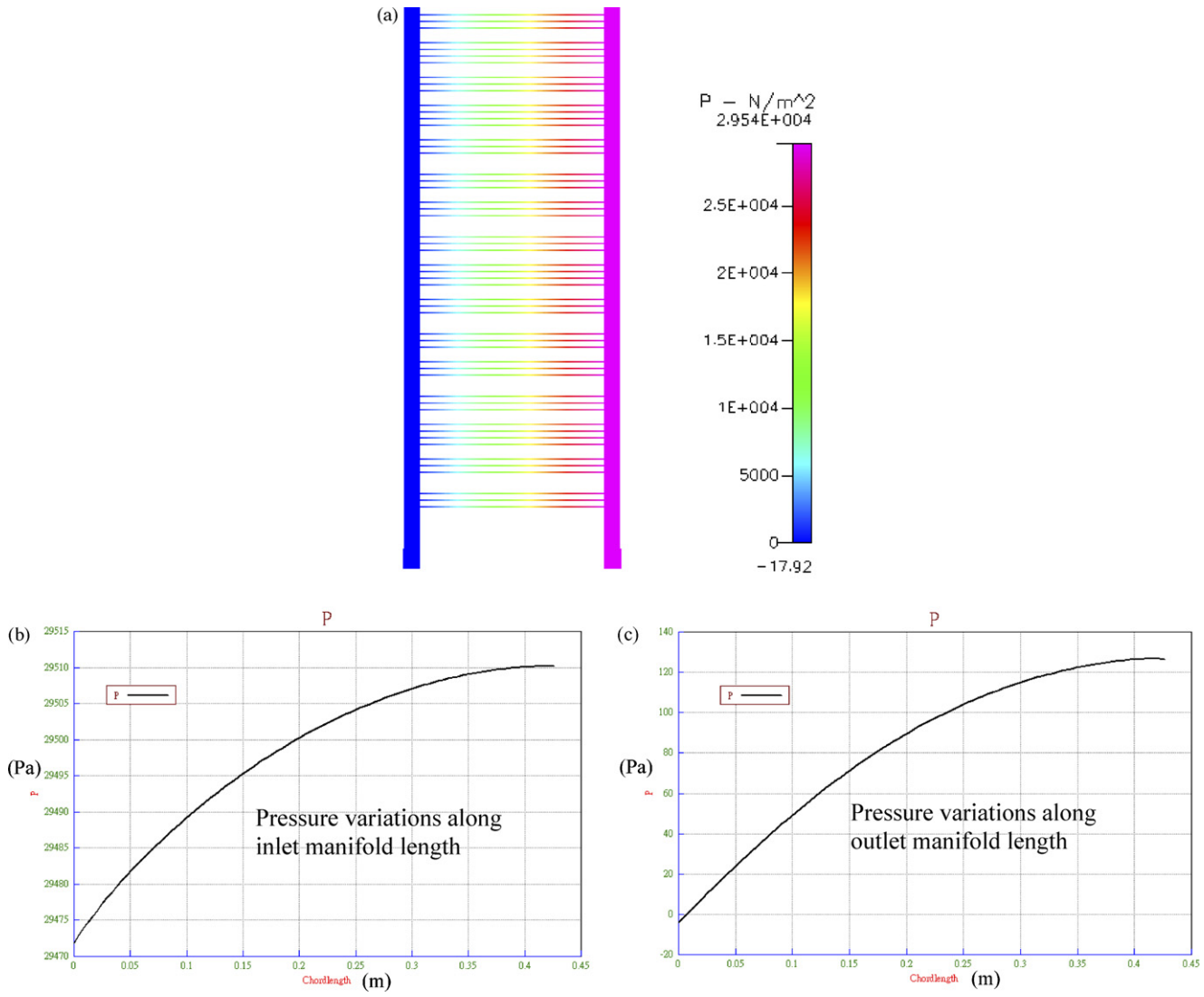

Fig. 3. (a) Stack flow pressure, (b) pressure variations along inlet manifold length, (c) pressure variations along outlet manifold length for case 2 ($K = 2.5 \times 10^{-10}$, $D = 12$ mm, 300 SLPM).

with unit: Pa (N m^{-2}). Pressure increases from the feeding end to the closed one of stacks at either inlet or outlet manifolds. Gas flow rate gradually decreases along inlet manifold length due to gas feeding into each cell. The decreased flow rate, i.e. decreased fluid velocity will cause a pressure gradient opposite to flow direction. For the outlet manifold, gas flow rate gradually increases from the closed end to the discharged one due to gas discharge from each cell. The increased flow rate, i.e. increased fluid velocity will cause a pressure gradient parallel to flow direction.

The pressure difference in manifolds is mainly associated with manifold width and is less dependent on the permeability, i.e. channel flow resistance. Larger manifold width causes a less pressure difference along the manifold length. By comparing cases with a width of 6 mm (case 1 and case 3) to cases with a width of 12 mm (case 2 and case 4), it shows that the pressure difference along the inlet manifold decreases from 140 Pa (case 1 and case 3) to 40 Pa (case 2 and case 4), and that along the outlet manifold from 550 Pa (case 1 and case 3) to 130 Pa (case 2 and case 4). This is because wider manifolds cause lower fluid velocity which leads to less pressure difference in manifolds.

The above analysis of manifold pressure difference shows that the outlet manifold contributes to a larger pressure difference than in the inlet one. This will cause an uneven pressure-drop in the cells, which will lead to uneven gas fed in each cell, i.e. an uneven flow distribution.

3.2. Momentum balance theories

Momentum balance theories [23] characterize overall momentum balance relationship consisting of momentum flux, pressure, and wall friction in a specific control volume. In the theories, net momentum flow rate must be equal to the sums of all forces, and the governing equation is:

$$\frac{D(\dot{m}\vec{V})}{Dt}|_{\text{sys}} = \sum \vec{F} \tag{9}$$

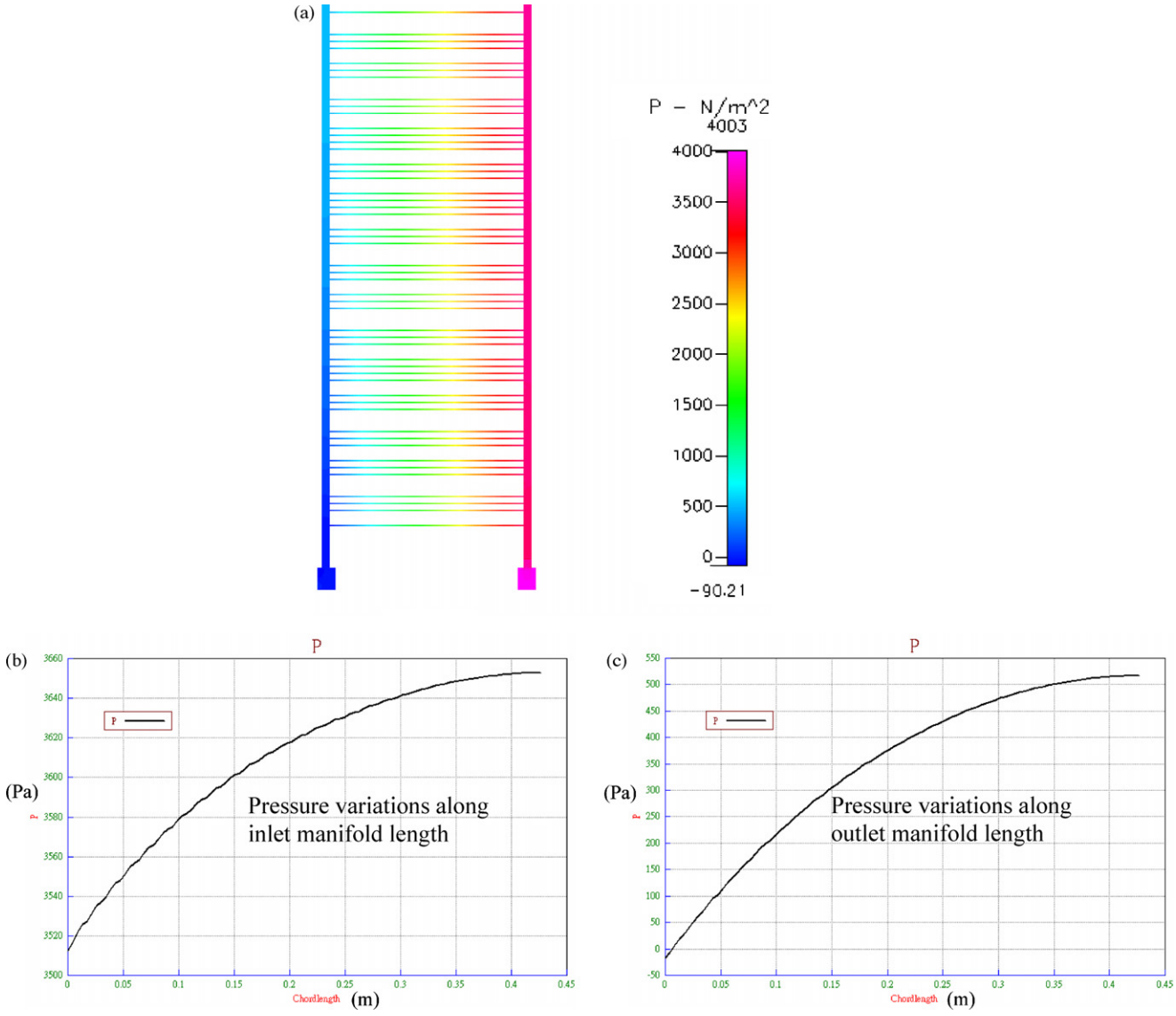

Fig. 4. (a) Stack flow pressure, (b) pressure variations along inlet manifold length, (c) pressure variations along outlet manifold length for case 3 ($K = 2.5 \times 10^{-9}$, $D = 6$ mm, 300 SLPM).

where $\dot{m}$ is mass flow rate, $\vec{V}$ is fluid velocity, and $\sum \vec{F}$ is the net value of all forces.

For steady flows, a momentum balance exists between net momentum flow rate, net forces of pressure and wall shear stress as follows:

$$\sum \dot{m}\vec{V} = \sum -P\vec{S} + \sum \vec{F}_{\mathrm{f}} \tag{10}$$

where P is pressure, $\vec{S}$ is pressure action area, and $\vec{F}_{\mathrm{f}}$ is wall shear stress.

Inlet and outlet manifolds are chosen as control volumes, as shown in Figs. 6 and 7, respectively. The two momentum-balance relationships are:

$$\begin{aligned} -\dot{m}V &= (P_1 - P_2)S - F_{\mathrm{f1}} = -\Delta P_{\mathrm{a}} S - F_{\mathrm{f1}} \\ &\Rightarrow \Delta P_{\mathrm{a}} = \frac{\dot{m}V - F_{\mathrm{f1}}}{S} \end{aligned} \tag{11}$$

$$\begin{aligned} \dot{m}V &= (P_4 - P_3)S - F_{\mathrm{f2}} = \Delta P_{\mathrm{b}} S - F_{\mathrm{f2}} \\ &\Rightarrow \Delta P_{\mathrm{b}} = \frac{\dot{m}V + F_{\mathrm{f2}}}{S} \end{aligned} \tag{12}$$

In the two equations, $\dot{m}V$ represents feeding momentum flow rate at the inlet manifold or discharging momentum flow rate at the outlet one. The F_{f1} and F_{f2} are friction force generated by fluid flow through inlet and outlet manifolds. The P_1 and P_2 are pressures at two ends of the inlet manifold, and P_3 and P_4 are pressures at two ends of the outlet one. The S is pressure action area. According to the momentum balance theories, the deviation between pressure difference in the inlet manifold: $\Delta P_{\mathrm{a}} = P_2 - P_1$ and that in the outlet manifold: $\Delta P_{\mathrm{a}} = P_4 - P_3$ is:

$$\Delta P_{\mathrm{a}} = \Delta P_{\mathrm{b}} - \frac{F_{\mathrm{f1}} + F_{\mathrm{f2}}}{S} < \Delta P_{\mathrm{b}} \tag{13}$$

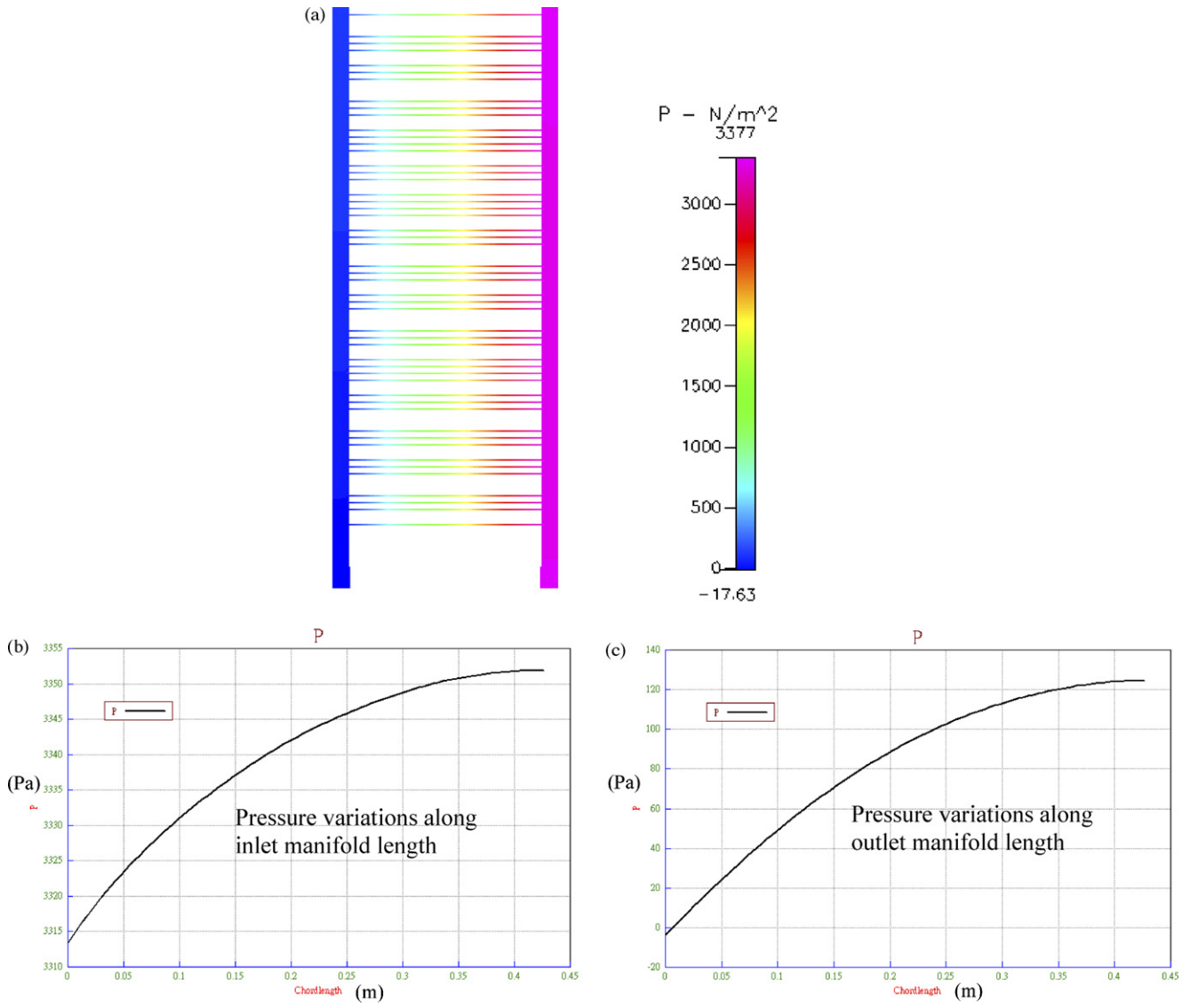

Fig. 5. (a) Stack flow pressure, (b) pressure variations along inlet manifold length, (c) pressure variations along outlet manifold length for case 4 ($K = 2.5 \times 10^{-9}$, $D = 12$ mm, 300 SLPM).

This theory could explain the higher pressure drop of the outlet manifold than the inlet manifold. Causes for the uneven pressure drop among the cells also could be explained.

3.3. Cell pressure drop and mass flow rate

In gas-distributed processes, forces caused by pressure gradients in channels drive the gas into each cell from the manifolds. In order to confirm that cell pressure drop dominates flow distribution, comparison between cell pressure drop and mass flow rate was studied.

Fig. 8 is a plot of cell pressure drop under 300 SLPM air feeding rate. A dimensionless pressure drop is implemented to progress comparisons between each case. It can be defined as follows:

$$\Delta\tilde{P} = \frac{\Delta P}{\Delta\bar{P}} = \frac{\Delta P}{\sum \Delta P/N} \tag{14}$$

where $\Delta\tilde{P}$ is dimensionless pressure drop, ΔP is cell pressure drop, $\Delta\bar{P} = \sum \Delta P/N$ is average cell pressure drop, and N is number of cells.

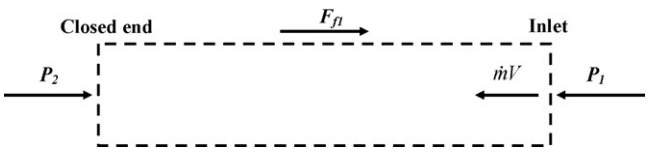

Fig. 6. Schematic representation of inlet manifold control volume.

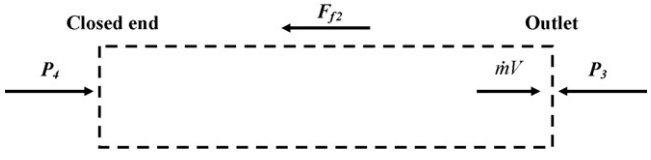

Fig. 7. Schematic representation of outlet manifold control volume.

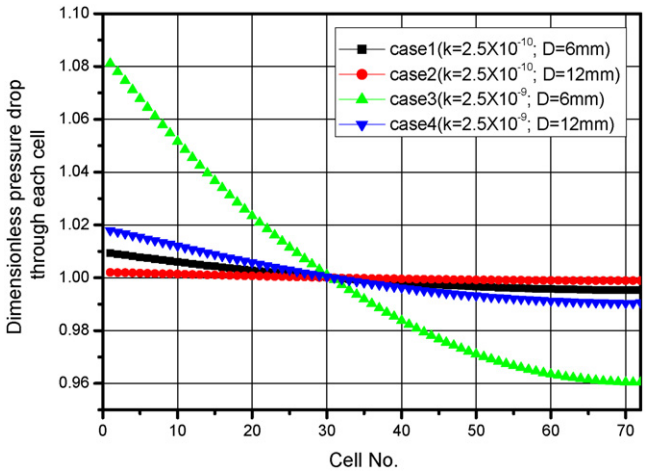

Fig. 8. Dimensionless cell pressure drop for each case (300 SLPM).

In plots of cell pressure drop, the x-coordinate indicates the cell number, where no. 1 is indicated as the cell at the feeding end and no. 72 as the cell at the closed one in stacks. The y-coordinate is defined as dimensionless pressure drop. The magnitude of dimensionless pressure drop for different cases are case 1: 1.009–0.995, case 2: 1.002–0.999, case 3: 1.081–0.960, case 4: 1.018–0.991. Dimensionless pressure-drop variation of all cases gradually decreases from the feeding end to the closed one in stacks. As for the uniform degree of pressure-drop distribution, the best one is case 2, and the next ones are case 1 and case 4, and the worst one is case 3.

The dimensionless mass flow rate in the individual cell for the 300 SLPM air feeding rate is given in Fig. 9. A dimensionless mass flow rate is implemented to compare the flow through the individual cells. It can be defined as follows:

$$\tilde{m} = \frac{\dot{m}}{\bar{\dot{m}}} = \frac{\dot{m}}{\dot{Q}/N} \tag{15}$$

where $\tilde{m}$ is dimensionless mass flow rate, $\dot{m}$ is cell mass flow rate, and $\bar{\dot{m}} = \dot{Q}/N$ is average cell mass flow rate, where $\dot{Q}$ is total mass flow rate of stacks and N is number of cells.

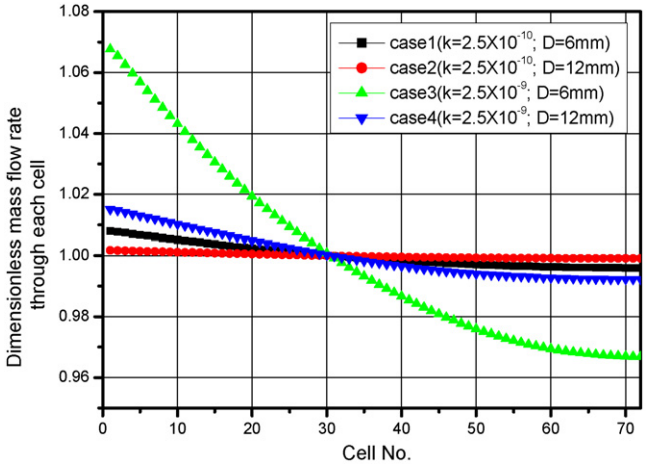

Fig. 9. Dimensionless cell mass flow rate for each case (300 SLPM).

In the plot of cell mass flow rate, the x-coordinate indicates the cell number, where no. 1 is the cell at the feeding end and no. 72 as the cell at the closed one in the stack. The y-coordinate is defined as dimensionless mass flow rate. The magnitude of dimensionless mass flow rate for the different cases are: case 1: 1.008–0.996, case 2: 1.002–0.999, case 3: 1.068–0.967 and case 4: 1.015–0.992. Variation of dimensionless mass flow rate for all cases gradually decreases from the feeding end to the closed one in stacks. Uniform degree of flow distribution is almost the same as that of pressure-drop variation. This confirms that the driving forces governing gas feed into each cell results from pressure drop in channels.

3.4. Analysis of flow distribution

A pressure drop model shown in Fig. 10 is constructed to investigate pressure variation where manifolds, channels and gas flow direction are indicated, respectively. Since flow pressure is defined relative to the outlet pressure, pressure at outlet ports is set to zero. (The red solid line indicates pressure drop of cell no. 1, i.e. ΔP_1; the red dotted line indicates pressure drop of cell no. n, i.e. ΔP_n, the green solid line indicates pressure difference along the inlet manifold length, i.e. ΔP_a; and the blue solid line indicates pressure difference along the outlet manifold length, i.e. ΔP_b.) The following relationship will be satisfied for pressure drop ΔP_n, ΔP_1, ΔP_a and ΔP_b:

$$\Delta P_n = \Delta P_1 + \Delta P_a - \Delta P_b \tag{16}$$

The above equation can evaluate qualitatively the effect of channel flow resistance and manifold width on flow distribution. The ratio of ΔP_n to ΔP_1 is calculated by using the relationship: $\Delta P_n = \Delta P_1 + \Delta P_a - \Delta P_b$ from pressure-drop model and $\Delta P_a < \Delta P_b$ from momentum balance theory respectively:

$$\frac{\Delta P_n}{\Delta P_1} = \frac{\Delta P_1 + \Delta P_a - \Delta P_b}{\Delta P_1} = 1 + \frac{\Delta P_a - \Delta P_b}{\Delta P_1} < 1 \tag{17}$$

The above equation defines the ratio of pressure drop of cell no. n to no. 1. This ratio is less than one, i.e. cell pressure drop decreases gradually from the feeding end to the closed one, and it also corresponds with the modeling results.

From the above discussion, it can be seen that the cell pressure drop dominates gas flow into each cell. Therefore, the ratio

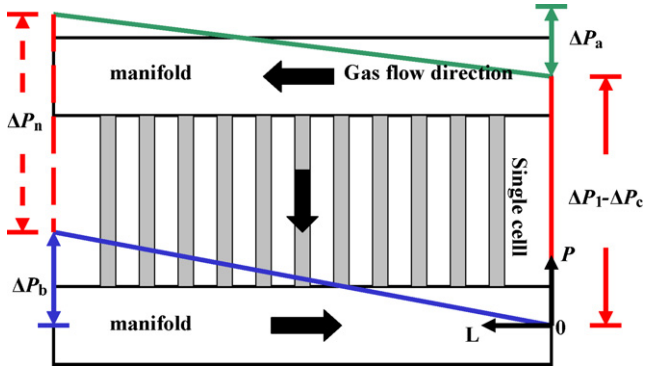

Fig. 10. Schematic representation of stack pressure drop model.

Table 2
Stack design parameters and corresponding pressure drop (300 SLPM)

Permeability	Manifold width			
	$D = 6$ mm		$D = 12$ mm	
$K = 2.5 \times 10^{-10}$ m^2	ΔP_a (Pa)	139	ΔP_a (Pa)	38
	ΔP_b (Pa)	550	ΔP_b (Pa)	130
	ΔP_1 (Pa)	29691	ΔP_1 (Pa)	29476
$K = 2.5 \times 10^{-9}$ m^2	ΔP_a (Pa)	140	ΔP_a (Pa)	39
	ΔP_b (Pa)	535	ΔP_b (Pa)	128
	ΔP_1 (Pa)	3530	ΔP_1 (Pa)	3316

between cell pressure drops can be qualitatively used to evaluate gas flow distribution. The ratio of mass flow rate of cell no. n to no. 1 can be defined as follows:

$$\frac{\dot{m}_n}{\dot{m}_1} \approx \frac{\Delta P_n}{\Delta P_1} = 1 - \frac{\Delta P_b - \Delta P_a}{\Delta P_1} \tag{18}$$

The above equation indicates the ratio of cell mass flow rate between the two cells which can be calculated with manifold pressure differences ΔP_a and ΔP_b and cell pressure drop ΔP_1. When this ratio is closer to one a more uniform flow distribution will occur in stacks. Next, this equation is implemented to analyze the above cases.

Model design parameters and contributed pressure drops under 300 SLPM air feeding rate are shown in Table 2. Pressure differences in the inlet and outlet manifold, i.e. ΔP_a and ΔP_b are dominated by manifold widths. Compared with manifold widths, permeability, i.e. channel flow resistance has a weaker influence on manifold pressure difference but dominates cell pressure drop. A decrease of one order magnitude in permeability will result an increase of one order magnitude of overall pressure drop. But variable manifold widths contribute almost nothing to overall pressure drop. The ratios of cell mass flow rate for each case under 300 SLPM air feeding rate are shown in Table 3 and no. n is defined as 72, where case 1 is 0.986, case 2 is 0.997, case 3 is 0.888, and case 4 is 0.973. The ratios of each case correspond qualitatively with the modeling results. As for the uniform degree of flow distribution, case 2 is the best one followed by case 1 and case 4 in turn and case 3 is the worst one.

From the above analysis, low permeability can contribute to a large cell pressure drop ΔP_1 and improve flow distribution. Large manifold width can cause less deviation between inlet and outlet manifold pressure difference, i.e. $\Delta P_b - \Delta P_a$ and then it also will improve flow distribution.

3.5. Flow distribution under low air feeding rate

The above cases are analyzed under 300 SLPM air feeding rate and the stack will generate 4–5 kW output power at these feeding rate. In order to study stack flow distribution for output power 1–2 kW, approximately 100 SLPM air feeding rate was selected for investigation. The inlet air velocity was 3 m s^{-1} at 100 SLPM air feeding rate. Besides the air feeding rate, stack model parameters and modeling conditions are the same as the above cases. In this section, the difference of flow distribution under different air feeding is studied by momentum balance theories and the influences of channel resistance and manifold width on flow distribution are analyzed.

Flow pressure variation for case 1, case 2, case 3 and case 4 under 100 SLPM air feeding rate are shown in Figs. 11–14(a)–(c), respectively where (a) is overall flow pressure in stacks and (b) and (c) are respectively average pressure variation along inlet and outlet manifold length.

Under 100 SLPM air feeding, overall pressure drop of different cases is case 1 > case 2 > case 3 > case 4. This is because larger channel flow resistance contributes to a larger overall pressure drop. While manifold width is enhanced lower fluid velocity contributes to less pressure drop.

Pressure increases from the feeding end to the closed one in stacks at either inlet or outlet manifolds. Decreased fluid velocity from the feeding end to the closed one along the inlet manifold length will cause a pressure gradient opposite to flow direction. For the outlet manifold, increased fluid velocity from the closed end to the feeding one will cause a pressure gradient parallel to velocity direction.

Overall pressure drops of each case under 100 and 300 SLPM air feeding rate are shown in Table 4.

Since channel flow resistance, i.e. permeability contributes largely to flow pressure drop, the correlation between pressure gradient, flow velocity and permeability can be approximated with the equation: $\nabla p \approx \phi \mu U/K$. From this equation, overall pressure drop is roughly proportional to air feed, i.e. the ratio of overall pressure drop for 300 SLPM to that for 100 SLPM is about 3. For realistic channels, such as parallel, serpentine, or Z pattern channel pressure drop is also roughly proportional to flow velocity. ‘, channel flow resistance approximated by permeability is satisfied qualitatively with governing mechanism of channel pressure drop.

Fig. 15 is a plot of cell pressure drop under 100 SLPM air feeding rate. A dimensionless pressure drop is implemented to progress comparisons between each case. Cell pressure drops of each case under 100 and 300 SLPM air feeding rate are shown in Table 5.

Table 3
The ratio of cell mass flow rate for each case (300 SLPM)

Case	Ratio
1	0.986
2	0.997
3	0.888
4	0.973

Table 4
Overall pressure drops of each case under 100 and 300 SLPM air feeding rate

Air feeding rate	100 SLPM (Pa)	300 SLPM (Pa)
Case 1	9468	30160
Case 2	9430	29540
Case 3	1090	4003
Case 4	1052	3377

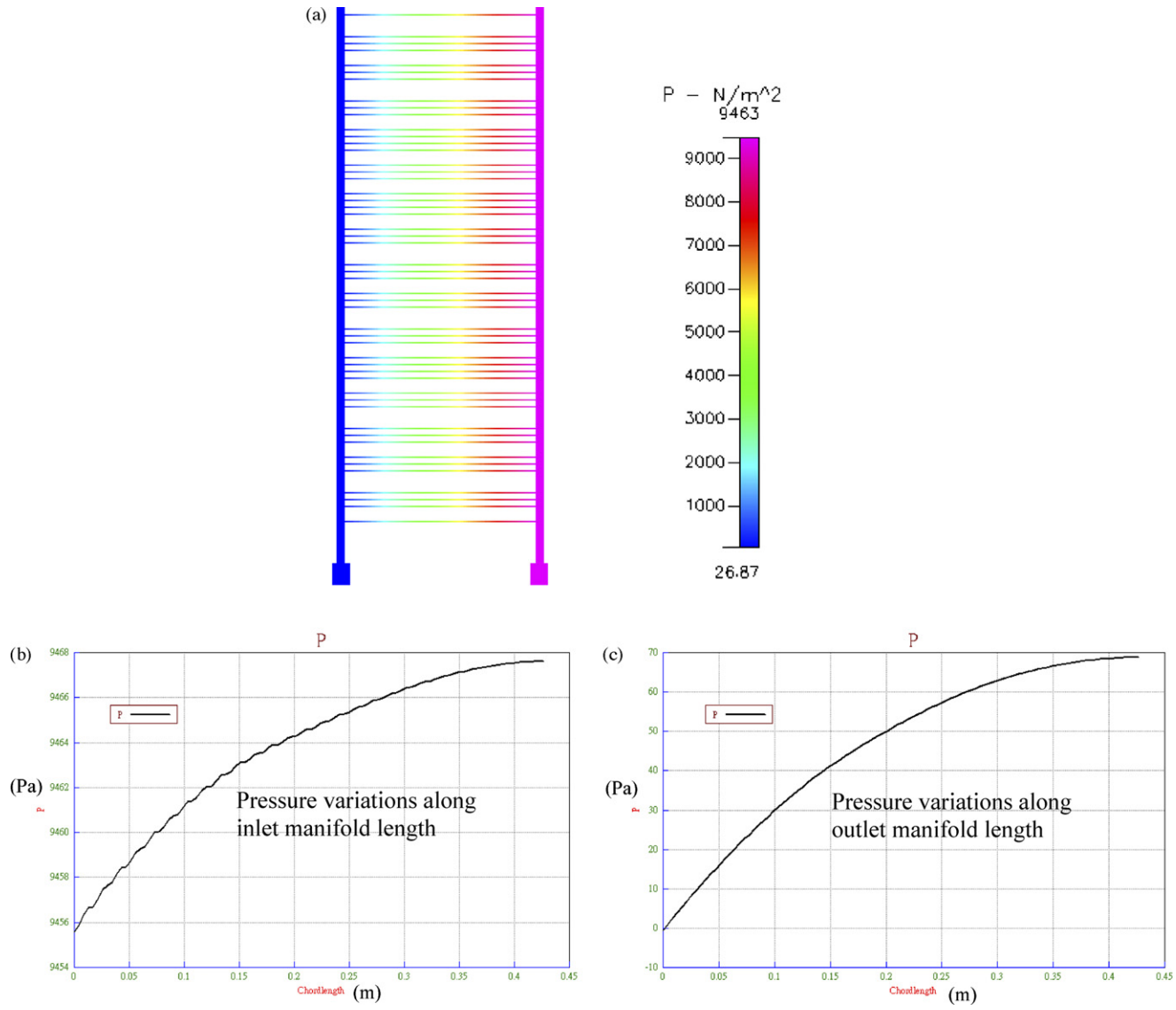

Fig. 11. (a) Stack flow pressure, (b) pressure variations along inlet manifold length, (c) pressure variations along outlet manifold length for case 1 ($K = 2.5 \times 10^{-10}$, $D = 6$ mm, 100 SLPM).

Under different air feed dimensionless pressure-drop variation of all cases gradually decrease from the feeding end to the closed one in stacks. As for the uniform degree of pressure-drop distribution, the best one is case 2 and the next are case 1 and case 4 in turn, and the worst one is case 3. In addition, lower air feed will cause more uniform cell pressure-drop variation, and this will also cause more uniform flow distribution.

Fig. 16 is a plot of cell mass flow rate under 100 SLPM air feeding rate. A dimensionless cell mass flow rate is implemented to study comparisons between each case. Cell mass flow rate of each case under 100 and 300 SLPM air feeding rate are shown in Table 6.

Under different air feed variation of dimensionless mass flow rate of all cases gradually decreases from the feeding end to the closed one in stacks. Uniform degree of flow distribution is almost the same as that of pressure-drop distribution and lower air feed indeed causes more uniform distribution of cell flux.

Table 5
Cell pressure drops of each case under 100 and 300S LPM air feeding rate

Air feeding rate	100 SLPM	300 SLPM
Case 1	1.004–0.998	1.009–0.995
Case 2	1.0008–0.9996	1.002–0.999
Case 3	1.036–0.983	1.081–0.960
Case 4	1.007–0.996	1.018–0.991

Table 6
Cell mass flow rate of each case under 100 and 300 SLPM air feeding rate

Air feeding rate	100 SLPM	300 SLPM
Case 1	1.004–0.998	1.008–0.996
Case 2	1.0008–0.9996	1.002–0.999
Case 3	1.034–0.984	1.068–0.967
Case 4	1.007–0.997	1.015–0.992

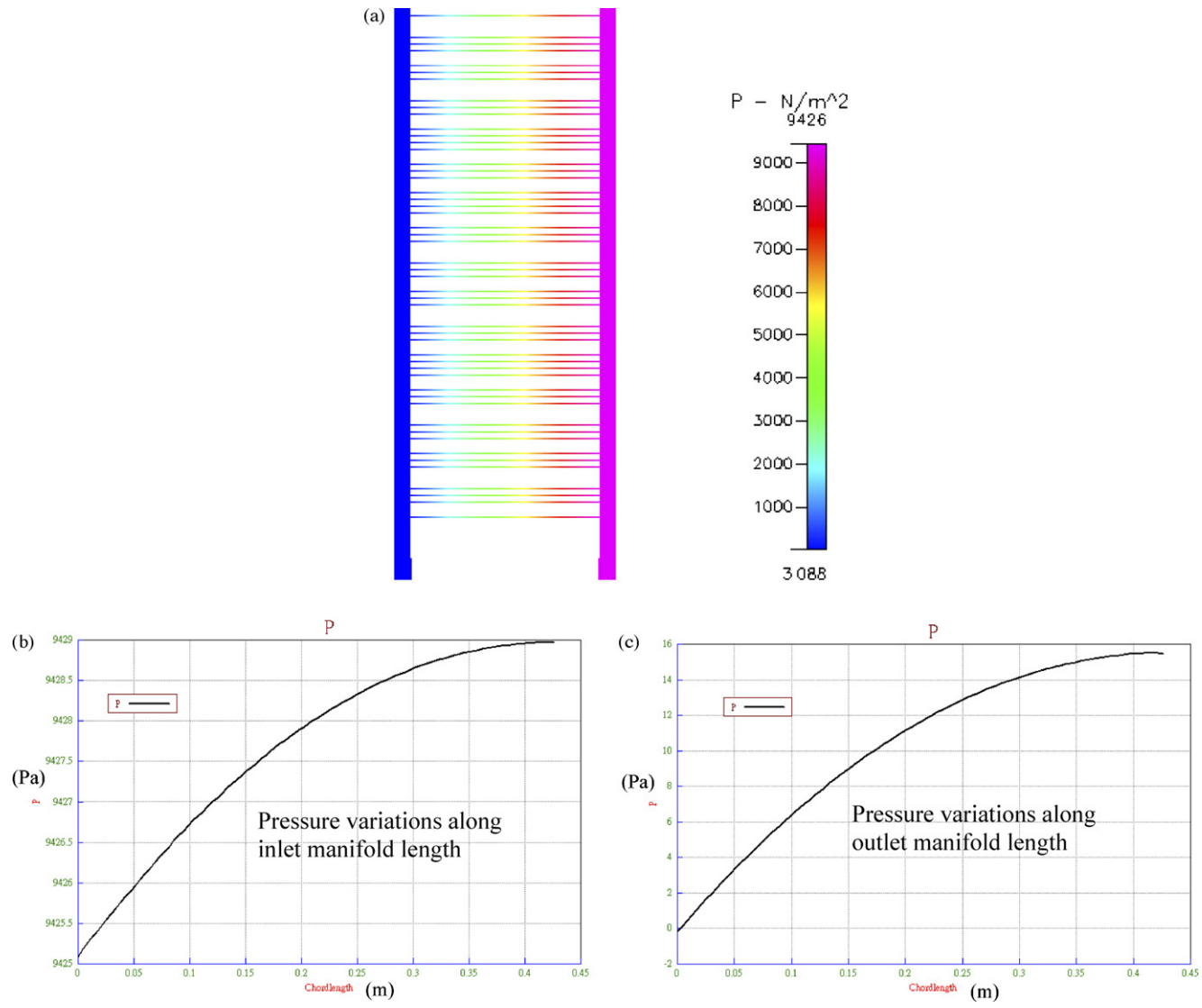

Fig. 12. (a) Stack flow pressure, (b) pressure variations along inlet manifold length, (c) pressure variations along outlet manifold length for case 2 ($K = 2.5 \times 10^{-10}$, $D = 12$ mm, 100 SLPM).

Momentum balance theories are used to study the difference of flow distribution under different air feed and the influence of channel resistance and manifold width on flow distribution. The ratio of mass flow rate of cell no. n to no. 1 can be defined with manifold pressure differences ΔP_a and ΔP_b and cell pressure drop ΔP_1 as follows:

$$\frac{\dot{m}_n}{\dot{m}_1} \approx \frac{\Delta P_n}{\Delta P_1} \approx 1 - \frac{\Delta P_b - \Delta P_a}{\Delta P_1} \tag{19}$$

Channel pressure drop ΔP_1 is approximately proportional to flow velocity, i.e. $\Delta P_1 \propto V$. However, manifold pressure differences ΔP_a and ΔP_b are roughly proportional to the square of flow velocity, i.e. ΔP_a or $\Delta P_b \propto V^2$. This is because manifold pressure differences $\Delta P_a = \dot{m}V - F_{f1}/S$ and $\Delta P_b = \dot{m}V - F_{f2}/S$ can be derived respectively as follows:

$$\Delta P_a = \frac{\dot{m}V - F_{f1}}{S} \approx \frac{\rho V^2 - \sum k_1 V^2/2}{S} \propto V^2 \tag{20}$$

$$\Delta P_b = \frac{\dot{m}V + F_{f2}}{S} \approx \frac{\rho V^2 + \sum k_2 V^2/2}{S} \propto V^2 \tag{21}$$

where momentum flux is proportional to the square of flow velocity. According to fluid mechanics theories [24], friction forces are approximated as multiplication of friction coefficient and the square of flow velocity, i.e. $F_f \approx kV^2/2$, where k is friction coefficient. Therefore, the manifold pressure difference is also proportional to the square of flow velocity.

Model design parameters and contributed pressure drop under 100 SLPM air feeding rate are shown in Table 7. By comparing Table 4 to Table 2, cell pressure drop under 300 SLPM air feeding rate is three times larger than that under 100 SLPM one, and manifold pressure difference under 300 SLPM air feeding rate is nine times larger than that under 100 SLPM one. This corresponds to conclusions derived from momentum balance theories. While the air feed is varied and the other parameters are fixed, the equation: $\frac{\dot{m}_n}{\dot{m}_1} \approx \frac{\Delta P_n}{\Delta P_1} \approx 1 - \frac{\Delta P_b - \Delta P_a}{\Delta P_1}$ can be described

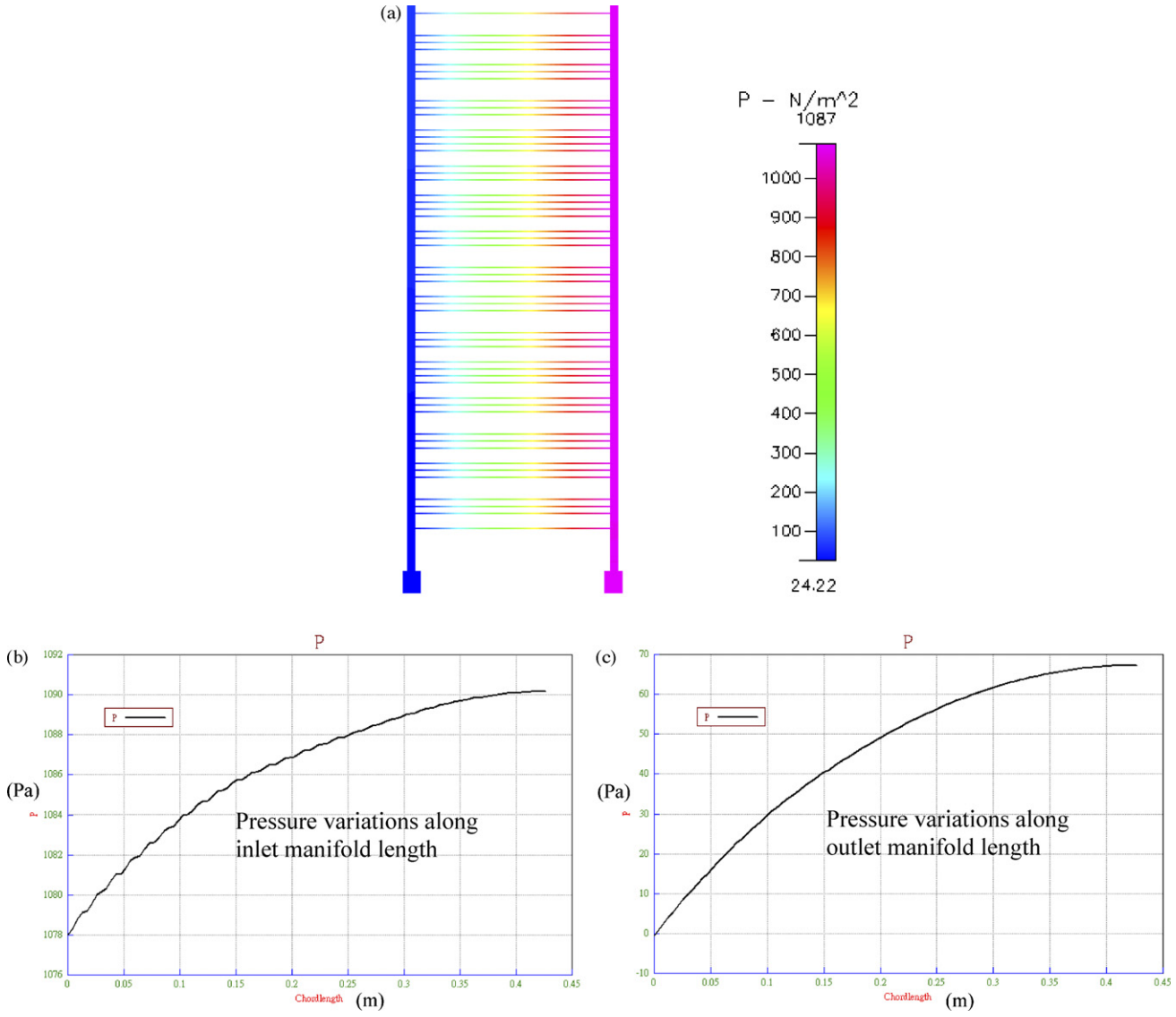

Fig. 13. (a) Stack flow pressure, (b) pressure variations along inlet manifold length, (c) pressure variations along outlet manifold length for case 3 ($K = 2.5 \times 10^{-9}$, $D = 6$ mm, 100 SLPM).

with a flow velocity function as follows:

$$\frac{\dot{m}_n}{\dot{m}_1} \approx 1 - \frac{\Delta P_b - \Delta P_a}{\Delta P_1} = 1 - \frac{f_1(V^2)}{f_2(V)} = 1 - f(V),$$
$$\text{where} \quad f(V) \propto V \tag{22}$$

Table 7
Stack design parameters and corresponding pressure drop (100 SLPM)

Permeability	Manifold width			
	$D = 6$ mm		$D = 12$ mm	
$K = 2.5 \times 10^{-10}$ m^2	ΔP_a (Pa)	12	ΔP_a (Pa)	4
	ΔP_b (Pa)	69	ΔP_b (Pa)	16
	ΔP_1 (Pa)	9456	ΔP_1 (Pa)	9425
$K = 2.5 \times 10^{-10}$ m^2	ΔP_a (Pa)	12	ΔP_a (Pa)	4
	ΔP_b (Pa)	68	ΔP_b (Pa)	15
	ΔP_1 (Pa)	1078	ΔP_1 (Pa)	1048

When the air feed is reduced, decreased flow velocity makes $f(V)$ smaller to lead the ratio: $\dot{m}_n/\dot{m}_1$ to approach close to one. By comparing Table 5 to Table 3, flow distribution under 100 SLPM air-feeding rate is more uniform. The ratios of cell mass flow rate for each case in Table 8 are, case 1: 0.986, case 2: 0.997, case 3: 0.888, and case 4: 0.973. The ratios qualitatively correspond to variations of cell mass flow rate in Fig. 16. As for each design parameter, low permeability contributes to a large cell pressure drop ΔP_1 and improves flow distribution. Large

Table 8
The ratio of cell mass flow rate for each case (100 SLPM)

Case	Ratio
1	0.994
2	0.999
3	0.948
4	0.990

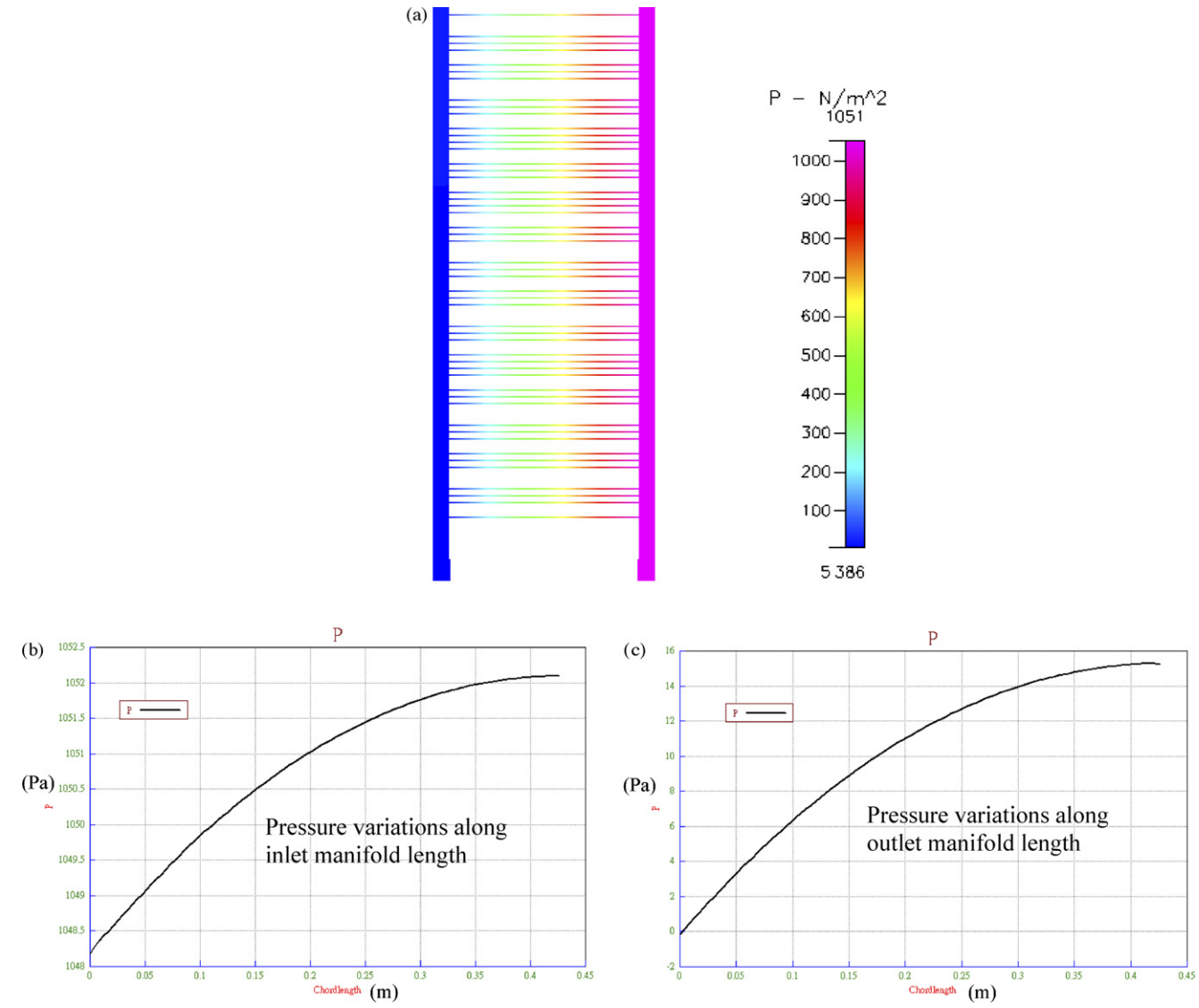

Fig. 14. (a) Stack flow pressure, (b) pressure variations along inlet manifold length, (c) pressure variations along outlet manifold length for case 4 ($K = 2.5 \times 10^{-9}$, $D = 12$ mm, 100 SLPM).

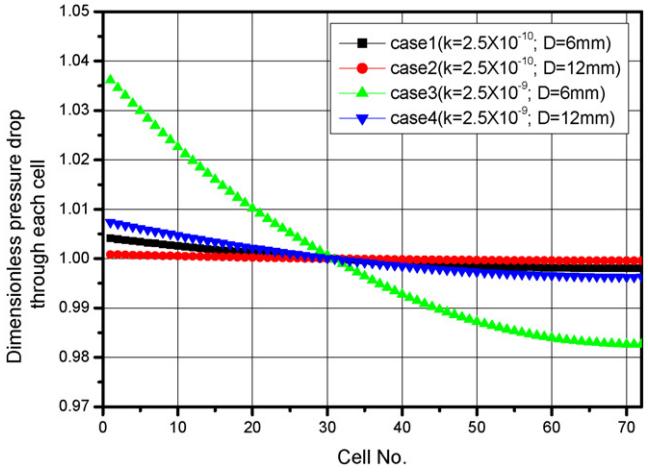

Fig. 15. Dimensionless cell pressure drop for each case (100 SLPM).

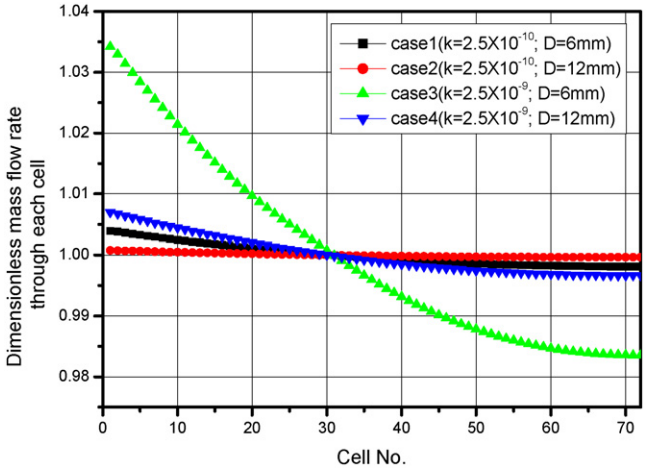

Fig. 16. Dimensionless cell mass flow rate for each case (100 SLPM).

manifold width causes a less deviation between the inlet and outlet manifold pressure difference, i.e. $\Delta P_b - \Delta P_a$ and then also improves flow distribution.

4. Conclusions

A fuel-cell stack model is constructed using computational fluid dynamics to investigate pressure variation, flow distribution for different channel flow resistance, manifold widths and air feed. Proposed momentum balance theories and pressure-drop model can be used to qualitatively investigate the flow distribution occurred in stacks.

Following are the conclusions of this study.This study evaluates flow distribution with a pressure-drop model and explains the physical mechanism governing this phenomenon qualitatively.Different air feed will cause different flow distribution. This study indicates that lesser air feed promotes more uniform flow distribution than higher air feed. This is because there exist different governing mechanisms between manifold pressure difference and channel pressure drop from momentum balance theories and pressure-drop model.Different channel design in stacks will affect flow distribution. Channels with large flow resistance contribute more pressure drop, and then cause a more uniform flow distribution. Therefore, channel design with large flow resistance is advantageous for flow distribution.While manifold widths increase, a more uniform flow distribution will be achieved. For manifold design in stacks, its width should be enhanced as much as possible and this is also beneficial for lowering overall stack pressure drop.The important points to be considered in stack design are lowering overall pressure drop and attaining high performance and stable operation. However, competitions and conflict always exist between these performance characteristics. In order to satisfy multiphase requirements of stack design, enhanced manifold size is a better solution to promote flow distribution and implement flow-field optimal design of fuel-cell stacks.

References

[1] J. Larminie, A. Dicks, Fuel cell Systems Explained, Wiley, 2002.
[2] D.M. Bernardi, M.W. Verbrugge, AICHE J. 37 (1991) 1151–1163.
[3] D.M. Bernardi, M.W. Verbrugge, J. Electrochem. Soc. 139 (1992) 2477–2491.
[4] T.E. Springer, T.A. Zawodzinski, S. Gottesfeld, J. Electrochem. Soc. 138 (1991) 2334–2342.
[5] T.V. Nguyen, R.E. White, J. Electrochem. Soc. 140 (1993) 2178–2186.
[6] V. Gurau, H. Liu, S. Kakac, AICHE J. 44 (1998) 2410–2421.
[7] S. Um, C.Y. Wang, J. Power Sources 125 (2004) 40–51.
[8] H. Meng, C.Y. Wang, ChES 59 (2004) 3331–3343.
[9] U. Pasaogullari, C.Y. Wang, Electrochim. Acta 49 (2004) 4359–4369.
[10] H. Ju, H. Meng, C.Y. Wang, Int. J. Heat Mass Transfer 48 (2005) 1303–1315.
[11] Y. Wang, C.Y. Wang, J. Power Sources 147 (2005) 148–161.
[12] Y. Wang, C.Y. Wang, J. Power Sources 153 (2006) 130–135.
[13] T. Berning, D.M. Lu, N. Djilali, J. Power Sources 106 (2002) 284–294.
[14] T. Berning, N. Djilali, J. Power Sources 124 (2003) 440–452.
[15] P.T. Nguyen, T. Berning, N. Djilali, J. Power Sources 130 (2004) 149–157.
[16] J.H. Koh, H.K. Seo, C.G. Lee, Y.S. Yoo, H.C. Lim, J. Power Sources 115 (2003) 54–65.
[17] G. Karimi, J.J. Baschuk, X. Li, J. Power Sources 147 (2005) 162–177.
[18] X. Yu, B. Zhou, A. Sobiesiak, J. Power Sources 147 (2005) 184–195.
[19] K. Promislow, Brian Wetton, J. Power Sources 150 (2005) 129–135.
[20] M.H.J. Pedras, M.J.S. de Lemos, Int. J. Heat Mass Transfer 44 (2001) 1081–1093.
[21] J.P. Van Doormaal, F.D. Raithby, Numer. Heat Transfer 7 (1984) 147–163.
[22] S.V. Patankar, Numerical Heat Transfer and Fluid Flow, Hemisphere Publishing Corporation, 1978.
[23] K. Nanbu, S. Igarashi, Vacuum 21 (1992) 221–228.
[24] R.W. Fox, A.T. McDonald, Introduction to Fluid Mechanics, Wiley, 1994.